Received 17 July 2021; revised 15 August 2021; accepted 23 August 2021. Date of publication 27 August 2021; date of current version 7 September 2021.
The review of this article was arranged by Editor K. Shenai.

Digital Object Identifier 10.1109/JEDS.2021.3108159

Modeling and Analysis of Double Channel GaN HEMTs Using a Physics-Based Analytical Model

RASIK RASHID MALIK [1] (Graduate Student Member, IEEE), MEHAK ASHRAF MIR [1], ZARAK BHAT [1], AHTISHAM PAMPORI [2] (Graduate Student Member, IEEE), YOGESH SINGH CHAUHAN [2] (Fellow, IEEE), AND SHEIKH AAMIR AHSAN [1] (Member, IEEE)

1 Nanoelectronic Research and Development Laboratory, Department of Electronics and Communication Engineering, National Institute of Technology Srinagar, Srinagar 190006, India
2 Nanolab, Department of Electrical Engineering, Indian Institute of Technology Kanpur, Kanpur 208016, India

CORRESPONDING AUTHOR: R. R. MALIK (e-mail: rasik_04phd19@nitsri.ac.in)

This work was supported in part by DST-Science and Engineering Research Board Startup Research Grant under Award SRG/2019/001122.

ABSTRACT In this work, we report the development of a new physics-based analytical model for current and charge characteristics of Double Channel (DC) Gallium Nitride High Electron Mobility Transistors (GaN-HEMTs). The model has at its core the self-consistent calculation of the charge densities, for both upper and lower channels, obtained from a solution of the Schrödinger and Poisson equations. Fermi-Dirac (FD) distribution together with 2D density of states is used for mobile carrier statistics in both the channels. Furthermore, drift-diffusion transport is used to compute the channel current using charge densities at channel extremities. Finally, the model is validated against TCAD simulation and experimental data for a DC-GaN-HEMT. The model, by virtue of its fully physics-based nature, precisely captures the charge screening effect in the lower channel without invoking any empirical clamping functions, unlike prior models, and also possesses the feature of being geometrically scalable.

INDEX TERMS GaN HEMTs, Schrödinger–Poisson, charges, compact model, double-channel, drift-diffusion, capacitance.

I. INTRODUCTION

Gallium Nitride High Electron Mobility Transistors (GaN HEMTs) have emerged as strong contenders for power electronics and radio frequency (RF) applications [1], however, as a manifestation of a strong spontaneous and piezoelectric polarization, GaN HEMTs are essentially depletion-mode type in nature. To this end, GaN experimentalists have proposed several approaches such as a recessed-gate [2], p-cap gate [3], AlTiO gate [4], fluorine plasma ion implantation [5], etc. so as to obtain normally-off operation in GaN devices.

Within these approaches, the metal oxide semiconductor HEMTs (MOS-HEMTs) with partially or fully recessed gates are favored due to compatibility of contemporary gate driver integrated circuits (ICs) with the conventional MOS-gates in comparison to the junction-based structures such as the p-GaN gate or Schottky-gate variants [6], [7]. The partially recessed gate maintains the high-mobility of electrons at the heterojunction underneath the gate, thereby maintaining a low R_{ON}. However, the threshold voltage (V_{th}) being sensitive to the recess depth, becomes susceptible to variability and therefore poses serious challenges in precisely controlling the R_{ON}. Conversely, fully recessed gate structures provide precise V_{th} control, nevertheless the carrier mobility is degraded as a result of the etching-induced damages and an inferior oxide/GaN interface, together leading to a significant increase in R_{ON} [8].

To circumvent the above cited challenges, double-channel (DC) MOS-HEMTs have been demonstrated as a possible work-around. Although DC-GaN-HEMTs were originally conceived for broadband voltage tunable terahertz detector and modulator applications due to plasmonic resonant absorption [9]; their enhancement-mode operation due to a fully recessed-gate at the upper channel complemented with a higher mobility due to channel-to-channel coupling [10], [11] has sought the attention of power device enthusiasts. Moreover, the lower channel maintains a high mobility due to its physical separation from the etched surface.

In order to fully comprehend the experimental characteristics of these devices and to harness their full potential in power-electronic circuit design, thorough understanding of their operation along with a guiding principle for optimal device design is of paramount importance, which necessitates the need to have a fully physics-based analytical compact model for DC-GaN-HEMTs. While several models have been reported for single-channel GaN-HEMTs which includes the state-of-the-art industry standard ASM-GaN-HEMT [12]–[17] and MVSG-GaN [18]–[20] models, only a handful of attempts have been made to model DC-GaN-HEMTs [21]–[23]. Wei *et al.* proposed an analytical model for DC-GaN-HEMTs that only takes care of the electrostatics and as such is only validated against charge densities for both channels at multiple bias conditions [21]. Rahman *et al.* [22], [23], presented a rigorous investigation using the self-consistent Schrödinger–Poisson equations that also considers transport and therefore models current for multiple device dimensions. Nevertheless, the model is based on a polynomial approximation between the quasi-Fermi level (E_f) and the electron sheet charge density (n_s) and therefore is full of quadratic equations and a long list of fitting parameters which makes the parameter extraction relatively tedious and often ambiguous due to the non-physical nature of the parameters. Additionally, to simplify the derivation the model only employs drift for transport instead of the conventional drift-diffusion formalism. Moreover, the model in [23] uses an empirical Gaussian distribution function for the lower channel charge density to replicate the charge screening effect at the onset of the upper channel.

In this article, we aim to present a fully physics-based analytical model for DC-GaN-HEMTs that overcomes these limitations of the prior models. The remainder of the paper is arranged as follows. In Section II, we introduce the model development for electrostatics and follow it up by the derivation of the drift-diffusion drain current in Section III. In Section IV, we validate the model against TCAD and experimental data with additional discussion on results. Finally, we conclude the article in Section V.

II. ELECTROSTATICS

A. DEVICE STRUCTURE CONSIDERED FOR MODEL DEVELOPMENT

A representative schematic of a typical DC-GaN-HEMT used in this work for model development is shown in Fig. 1. The structure uses a sapphire (Al_2O_3) substrate upon which two sequential undoped GaN layers are grown that are separated by a thin AlN insertion layer in between them. The structure also employs a recessed gate technique while using Al_2O_3 as the gate oxide. Al_2O_3, stacked upon a SiN layer, is also used for passivation in the access regions between the source and drain contacts that are placed over thin AlGaN barrier layers on either side of the channel. The values assigned to the parameters listed in Table 1 that are used in the model development are obtained from the experimental and simulation works mentioned in the literature [10], [11], [21],

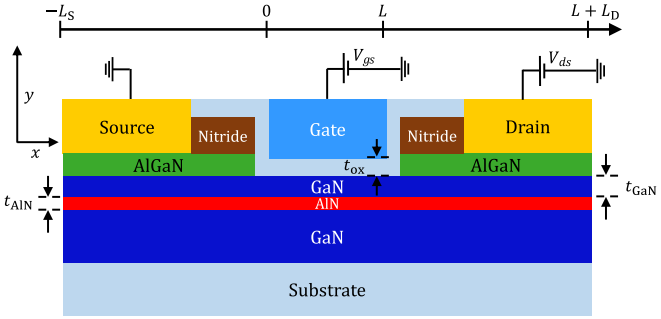

FIGURE 1. Cross-sectional schematic representation of the DC-GaN-HEMT used for model derivation in this article. The structure uses a recessed gate technique with Al_2O_3 as a gate oxide. Undoped GaN layers are placed on top of the sapphire substrate and separated by a thin AlN insertion layer.

TABLE 1. Description of symbols used in Fig. 1 and Fig. 2.

Symbol	Description	Value
t_{ox}	Thickness of Al_2O_3 gate dielectric	18 nm
t_{GaN}	Thickness of upper GaN layer	variable
t_{AlN}	Thickness of AlN layer	1.5 nm
L	Intrinsic gate length	1.5 μm
$\phi_{m,ox}$	Surface barrier height at the gated region	3.47 V
$\chi_{GaN,ox}$	Conduction band offset at the Al_2O_3/GaN interface	1.87 V
n_{buf}	Density of space charge in the buffer	0.6×10^{12} /cm^2
n_{it}	Density of interface charges	1.5×10^{13} /cm^2
$\sigma_{sp,GaN}$	GaN spontaneous polarization charge density	2.9×10^{-6} C/cm^2
$\sigma_{sp,AlN}$	AlN spontaneous polarization charge density	8.1×10^{-6} C/cm^2
$\sigma_{pz,AlN}$	AlN piezoelectric polarization charge density	5.05×10^{-6} C/cm^2

and [26]. Spontaneous and piezoelectric polarization charges in different layers are calculated according to [24]. Due to material defects, fixed charges due to the dangling bonds at the GaN/oxide interface, mobile charges under stress conditions, oxide-trapped charges created by X-ray radiation or hot-electron injection and other charges at the GaN/oxide interface or inside the oxide layer are represented by the net interface charge density, n_{it} [25].

B. BAND-DIAGRAM AND POTENTIAL BALANCE

The corresponding band-diagram and charge distribution, sketched along the negative y direction at any point x in the channel, is shown in Fig. 2 while the symbols used in the illustration are defined in Table 1. The sketch indicates the formation of 2DEG in both upper and lower triangular quantum wells induced due to polarization charges at the GaN/AlN/GaN interfaces. We start the model derivation by invoking charge neutrality in the entire structure, as we move along the gate to substrate direction, giving us

$$Q_g = -(qn_{it} - qn_u - \sigma_{GaN} - qn_l - qn_{buf}) \tag{1}$$

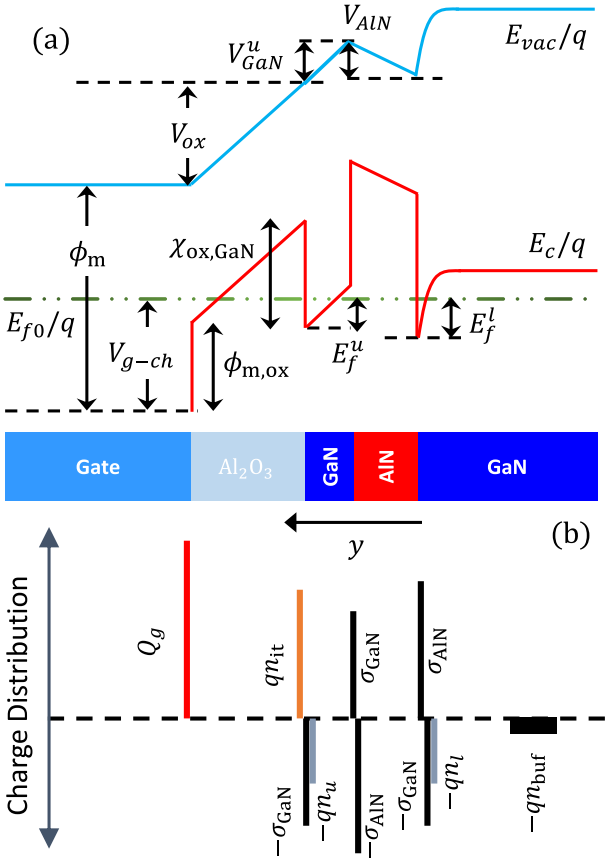

FIGURE 2. **(a) Band-diagram sketched along negative *y* direction at any *x* underneath the gate electrode. The symbols used in the diagram are defined in Table 1. (b) Illustration of corresponding charge distribution when both the channels are turned on. The 2DEG in each channel (n_u and n_l) is modeled as a sheet charge, and the electric field is assumed to be zero deep inside the substrate.**

where Q_g denotes the charge density at the gate electrode. We next solve the one-dimensional Poisson's equation for Fig. 2b to obtain the potential drops/gains across each layer, that are expressed as

$$V_{ox} = \frac{Q_g}{C_{\rm ox}} \tag{2}$$

$$V^u_{GaN} = \frac{Q_g + qn_{\rm it} - \sigma_{\rm GaN} - qn_u}{C_{\rm GaN}} \tag{3}$$

$$V_{AlN} = -\frac{Q_g + qn_{\rm it} - qn_u - \sigma_{\rm AlN}}{C_{\rm AlN}} \tag{4}$$

where V_{ox} ($C_{\rm ox}$), V^u_{GaN} ($C_{\rm GaN}$) and V_{AlN} ($C_{\rm AlN}$) are the voltages (areal capacitances) across the Al_2O_3, upper GaN and AlN layers respectively. We also use the one-dimensional Poisson's equation to calculate the electric fields at upper (Al_2O_3/GaN) and lower (AlN/GaN) interfaces, needed subsequently for sub-band calculations. The electric field values $\mathcal{E}^u_{GaN}$ and $\mathcal{E}^l_{GaN}$, obtained respectively for upper and lower channels, are

$$\mathcal{E}^u_{GaN} = \frac{Q_g + qn_{\rm it} - \sigma_{\rm GaN} - qn_u}{\epsilon_{\rm GaN}} = \frac{qn_l + qn_{\rm buf}}{\epsilon_{\rm GaN}} \tag{5}$$

$$\mathcal{E}^l_{GaN} = \frac{Q_g + qn_{\rm it} - qn_u - \sigma_{\rm GaN}}{\epsilon_{\rm GaN}} = \frac{qn_l + qn_{\rm buf}}{\epsilon_{\rm GaN}} \tag{6}$$

Henceforth, the symbol definitions of physical quantities used in the model derivation in the remainder of the article are described in Table 2. From an examination of the band-diagram in Fig. 2, doing the potential-balance from the gate electrode to the upper channel allows us to write

$$\phi_{\rm m,ox} - V_{g-ch} + V_{\rm ox} - \chi_{\rm GaN,ox} + \frac{E^u_f}{q} = 0 \tag{7}$$

Substituting V_{ox} from (2), we can rewrite (7) as

$$E^u_f = qV^u_{gov} + \frac{q(qn_{\rm it} - qn_u - \sigma_{\rm GaN} - qn_l - qn_{\rm buf})}{C_{\rm ox}} \tag{8}$$

where V^u_{gov} is defined as

$$V^u_{gov} = V_{g-ch} - \phi_{\rm m,ox} + \chi_{\rm GaN,ox} \tag{9}$$

We can redo the potential-balance from the gate electrode to the lower channel while using the voltage expressions from (2)-(4), to yield

$$E^l_f = qV^l_{gov} + \frac{q(qn_{\rm it} - qn_u - \sigma_{\rm GaN} - qn_l - qn_{\rm buf})}{C_{\rm ox}} + q(qn_{\rm it} - \sigma_{\rm GaN} - qn_l - qn_{\rm buf})\left(\frac{1}{C_{\rm GaN}} + \frac{1}{C_{\rm AlN}}\right) \tag{10}$$

where V^l_{gov} is defined as

$$V^l_{gov} = V_{g-ch} - \phi_{\rm m,ox} + \chi_{\rm GaN,ox} + \frac{\sigma_{\rm AlN}}{C_{\rm AlN}} + \frac{\sigma_{\rm GaN}}{C_{\rm GaN}} - qn_{\rm it}\left(\frac{1}{C_{\rm GaN}} + \frac{1}{C_{\rm AlN}}\right). \tag{11}$$

C. SCHRÖDINGER EQUATION AND FERMI-DIRAC STATISTICS

Fig. 2a indicates a triangular quantum well in each of the GaN layers at Al_2O_3/GaN and AlN/GaN interfaces. While the former is primarily due to the geometrical confinement of the electron sheet charge within a thin upper GaN layer, the latter results due to the electrical confinement caused by a strong polarization vector in AlN. Assuming quasi-constant electric fields $\mathcal{E}$ within these wells, the $j^{\rm th}$ sub-band energy E_j with respect to the conduction band edge can be obtained as the solution of the Schrödinger equation, and is approximated as [27]

$$E_j = q\left(\frac{\hbar^2}{2m^*}\right)^{\frac{1}{3}}\left(\frac{3}{2}\pi q\mathcal{E}\right)^{\frac{2}{3}}\left(j + \frac{3}{4}\right)^{\frac{2}{3}} \tag{12}$$

where m^* is the electron effective mass in GaN and $\hbar$ denotes the reduced Planck's constant. Considering only the first sub-band, the corresponding sub-bands for both the quantum wells are calculated as

$$E^{u(l)}_{c1} = \alpha\left(\mathcal{E}^{u(l)}_{GaN}\right)^{\frac{2}{3}} \tag{13}$$

where α is an experimentally determined parameter, which is equal to 2.1920×10^{-25} $\rm Kg^{\frac{1}{3}}m^{\frac{4}{3}}A^{\frac{2}{3}}$ for GaN with an electron

TABLE 2. Symbol description used in the model.

Symbol	Description
V_{g-ch}	Gate-to-channel potential difference at any point x
$D_{\rm e}$	2D Density of states
E_f	Position dependent quasi-Fermi level along y
E_f^u	Difference between the Fermi level and the conduction band of GaN at Al_2O_3/GaN interface
E_f^l	Difference between the Fermi level and the conduction band of GaN at AlN/GaN interface
E_{c1}^u	Difference between the first sub-band and the conduction band in the upper channel
E_{c1}^l	Difference between the first sub-band and the conduction band in the lower channel

effective mass of $0.22m_0$ [28]. Charge density expressions in each layer can now be obtained using the Fermi-Dirac statistics and 2-D density of states (DOS) under a parabolic dispersion relationship, as

$$n_{u(l)} = D_{\rm n} kT \ln\left[1 + \exp\left(\frac{E_f^{u(l)} - E_{c1}^{u(l)}}{kT}\right)\right] \tag{14}$$

where $D_{\rm n} = m^*/\pi\hbar^2$ is the 2-D DOS. Plugging in (5), (6), (8), (10) and (13) in the above equation, we arrive at (15) and (16), shown at the bottom of the page. Together they constitute a system of two non-linear equations with two unknowns n_u and n_l that are calculated self-consistently.

D. CHANNEL THRESHOLD VOLTAGES

The determination of the channel turn-on voltages in DC-MOS-HEMTs was previously carried out by Wei *et al.* [21]. Here, we follow the same approach and derive the expressions for threshold voltages for upper ($V_{\rm T}^{\rm u}$) and lower channel ($V_{\rm T}^{\rm l}$) as

$$V_{\rm T}^{\rm u} = \phi_{\rm m,ox} - \chi_{\rm GaN,ox} - \frac{qn_{\rm it} - \sigma_{\rm GaN} - qn_{\rm l0} - qn_{\rm buf}}{C_{\rm ox}} \tag{18}$$

$$V_{\rm T}^{\rm l} = \phi_{\rm m,ox} - \chi_{\rm GaN,ox} - \frac{\sigma_{\rm GaN}}{C_{\rm GaN}} - \frac{\sigma_{\rm AlN}}{C_{\rm AlN}} + \left(\frac{qn_{\rm it}}{C_{\rm GaN}} + \frac{qn_{\rm it}}{C_{\rm AlN}}\right) - (qn_{\rm it} - \sigma_{\rm GaN} - qn_{\rm buf})\left(\frac{1}{C_{\rm ox}} + \frac{1}{C_{\rm GaN}} + \frac{1}{C_{\rm AlN}}\right) \tag{19}$$

where $n_{\rm l0}$ stands for the lower channel charge density when V_{gs} is set to $V_{\rm T}^{\rm u}$, and is given by (17), shown at the bottom of the page. Since the lower channel is turned on before the upper channel [23], therefore, $V_{\rm T}^{\rm l}$ determines the effective threshold voltage of the overall device.

III. DRAIN-CURRENT MODEL

We now proceed to the computation of the drain current by invoking the drift-diffusion formalism for carrier transport under a gradual channel approximation [29]. The overall current density ($J = I/W$) at any point x along the channel, which is obtained as a sum of the individual current densities for each channel, after using the chain-rule can be written as

$$J = J_u + J_l = -\mu_{\rm nu} n_u \frac{dE_f}{dn_u}\frac{dn_u}{dx} - \mu_{\rm nl} n_l \frac{dE_f}{dn_l}\frac{dn_l}{dx} \tag{20}$$

where $\mu_{\rm n(u/l)}$ denotes the carrier mobility for upper/lower channel, assumed to be different the channels. While maintaining current continuity along the channel, integrating the above equation with limits $x : 0 \to L$, $n_u : n_{u,s} \to n_{u,d}$ and $n_l : n_{l,s} \to n_{l,d}$, we arrive at

$$I\frac{L}{W} = -\mu_{\rm nu}\int_{n_{u,s}}^{n_{u,d}} \left(n_u \frac{dE_f}{dn_u}\right) dn_u - \mu_{\rm nl}\int_{n_{l,s}}^{n_{l,d}} \left(n_l \frac{dE_f}{dn_l}\right) dn_l. \tag{21}$$

A. CALCULATION OF DERIVATIVES

As can be observed from (21), calculation of the overall drain current requires the derivatives of E_f with respect to

$$n_u = D_{\rm n} kT \ln\left[1 + \exp\left(\frac{qV_{gov}^u}{kT} + \frac{q(qn_{\rm it} - qn_u - \sigma_{\rm GaN} - qn_l - qn_{\rm buf})}{C_{\rm ox}kT} - \frac{\alpha}{kT}\left(\frac{qn_l + qn_{\rm buf}}{\epsilon_{\rm GaN}}\right)^{\frac{2}{3}}\right)\right] \tag{15}$$

$$n_l = D_{\rm n} kT \ln\left[1 + \exp\left(\frac{qV_{gov}^l}{kT} + \frac{q(qn_{\rm it} - qn_u - \sigma_{\rm GaN} - qn_l - qn_{\rm buf})}{C_{\rm ox}kT} + \frac{q(qn_{\rm it} - \sigma_{\rm GaN} - qn_l - qn_{\rm buf})}{kT}\left(\frac{1}{C_{\rm GaN}} + \frac{1}{C_{\rm AlN}}\right) - \frac{\alpha}{kT}\left(\frac{qn_l + qn_{\rm buf}}{\epsilon_{\rm GaN}}\right)^{\frac{2}{3}}\right)\right] \tag{16}$$

$$n_{\rm l0} = D_{\rm n} kT \ln\left[1 + \exp\left(\frac{V_{\rm tu} - \phi_{\rm m,ox} + \chi_{\rm GaN,ox} + \sigma_{\rm AlN}/C_{\rm AlN} + \sigma_{\rm GaN}/C_{\rm GaN} - qn_{\rm it}(1/C_{\rm GaN} + 1/C_{\rm AlN})}{kT/q} + \frac{q(qn_{\rm it} - \sigma_{\rm GaN} - qn_{\rm l0} - qn_{\rm buf})}{kT}\left(\frac{1}{C_{\rm ox}} + \frac{1}{C_{\rm GaN}} + \frac{1}{C_{\rm AlN}}\right) - \frac{\alpha}{kT}\left(\frac{qn_{\rm l0} + qn_{\rm buf}}{\epsilon_{\rm GaN}}\right)^{\frac{2}{3}}\right)\right] \tag{17}$$

n_u and n_l, which is accomplished by equating the expressions for E_f^u from (8) and (14) followed by substituting E_{c1}^u from (5) and (13), to get

$$qV_{gov}^u = kT\ln\left(\exp\left(\frac{n_u}{n_q}\right)-1\right)+\alpha\left(\frac{qn_l+qn_{buf}}{\epsilon_{GaN}}\right)^{\frac{2}{3}} - \frac{q(qn_{it}-qn_u-\sigma_{GaN}-qn_l-qn_{buf})}{C_{ox}} \quad (22)$$

where $n_q = D_n kT$. Using $qV_{gov}^u = qV_{go}^u + E_f$ in the above equation, where $V_{go}^u = V_g - \phi_{m,ox} + \chi_{GaN,ox}$, we can now differentiate it with respect to n_u, giving us

$$\frac{dE_f}{dn_u} = \frac{q^2}{C_{ox}}\left(1+\frac{dn_l}{dn_u}\right)+\frac{kT}{n_q}\frac{e^{n_u/n_q}}{e^{n_u/n_q}-1} + \frac{2q\alpha}{3\epsilon_{GaN}}\left(\frac{qn_l+qn_{buf}}{\epsilon_{GaN}}\right)^{-\frac{1}{3}}\frac{dn_l}{dn_u} \quad (23)$$

Following a similar procedure, derivative of E_f with respect to n_l can be obtained as

$$\frac{dE_f}{dn_l} = \frac{q^2}{C_{ox}}\left(1+\frac{dn_u}{dn_l}\right)+\frac{kT}{n_q}\frac{e^{n_l/n_q}}{e^{n_l/n_q}-1} + \frac{2q\alpha}{3\epsilon_{GaN}}\left(\frac{qn_l+qn_{buf}}{\epsilon_{GaN}}\right)^{-\frac{1}{3}}+q^2\left(\frac{1}{C_{GaN}}+\frac{1}{C_{AlN}}\right). \quad (24)$$

B. CURRENT CALCULATION

The above derived derivatives can be put in (21) to yield the complete form of the drain current density as shown in (25) at the bottom of the page. As can be observed, (25) is a summation of eight integral terms of which terms J_I, J_{II} and J_{III} are fairly straightforward and calculated as

$$J_I = -\frac{\mu_{nu}}{2L}\frac{q^2}{C_{ox}}\left(n_u^2\right)_{n_{u,s}}^{n_{u,d}}, \quad (26)$$

$$J_{II} = -\frac{\mu_{nl}}{2L}q^2\left(\frac{1}{C_{ox}}+\frac{1}{C_{GaN}}+\frac{1}{C_{AlN}}\right)\left(n_l^2\right)_{n_{l,s}}^{n_{l,d}}, \quad (27)$$

$$J_{III} = -\frac{\mu_{nl}\alpha}{5L}\left(\frac{q}{\epsilon_{GaN}}\right)^{\frac{2}{3}}\left[(n_l+n_{buf})^{\frac{2}{3}}(2n_l-3n_{buf})\right]_{n_{l,s}}^{n_{l,d}}. \quad (28)$$

The analytical transformation of terms J_{IV} and J_V is not as straightforward as in case of the prior terms, nonetheless, it can be performed using the procedure demonstrated by Marin *et al.* [30] as

$$J_{IV(V)} = -\frac{\mu_{nu(nl)}}{L}kT \times\left[\left(\frac{n_{u(l),s}^2-n_{u(l),d}^2}{2n_q}\right)+n_q\left(e^{-n_{u(l),s}/n_q}-e^{-n_{u(l),d}/n_q}\right)\right] \quad (29)$$

The remainder of the integrals in (25), that are cross-integral in nature, can be simplified, however, it requires the expression of n_u as an explicit function of n_l and vice-versa, as carried out in the Appendix, and expressed under as

$$n_u = n_q\ln\left[1+\exp\left(\frac{q^2(n_l-n_{l,s})}{kT}\left(\frac{1}{C_{GaN}}+\frac{1}{C_{AlN}}\right)+ \ln\left[e^{n_l/n_q}-1\right]-\ln\left[e^{n_{l,s}/n_q}-1\right]+\ln\left(e^{n_{u,s}/n_q}-1\right)\right)\right] \quad (30)$$

Plugging in n_u from (30) in J_{VII} and J_{VIII} leads us to their analytical forms. The integral in J_{VI} is solved by employing chain-rule in order to change the integration variable from n_u to n_l as

$$J_{VI} = -\frac{\mu_{nl}}{L}\frac{q^2}{C_{ox}}\int_{n_{l,s}}^{n_{l,d}} n_l\left(\frac{dn_u}{dn_l}\right)dn_l, \quad (31)$$

where dn_u/dn_l is calculated from (30).

IV. MODEL VALIDATION AND DISCUSSION

A. CHARGES AND THRESHOLD VOLTAGES

In Fig. 3, a comparison of the 2DEG density in the upper and the lower channels, as predicted by the model, is drawn against TCAD characteristics [21] as a function of V_{gs} for multiple t_{GaN} values. The model developed affirms the absence of 2DEG for zero bias, thereby enabling normally-off operation. Upon increasing V_{gs}, 2DEG formation is first witnessed in the lower channel followed by the turning on of the upper channel, as portrayed by different threshold voltages for n_u and n_l. Interestingly, the 2DEG density in the lower channel saturates at the onset of the upper channel which, upon turning on, screens the lower channel from

$$J = -\underbrace{\frac{\mu_{nu}}{L}\frac{q^2}{C_{ox}}\int_{n_{u,s}}^{n_{u,d}} n_u dn_u}_{J_I} - \underbrace{\frac{\mu_{nl}}{L}q^2\left(\frac{1}{C_{ox}}+\frac{1}{C_{GaN}}+\frac{1}{C_{AlN}}\right)\int_{n_{l,s}}^{n_{l,d}} n_l dn_l}_{J_{II}} - \underbrace{\frac{2\mu_{nl}q\alpha}{3\epsilon_{GaN}L}\int_{n_{l,s}}^{n_{l,d}}\left(\frac{qn_l+qn_{buf}}{\epsilon_{GaN}}\right)^{-\frac{1}{3}} n_l dn_l}_{J_{III}}$$
$$- \underbrace{\frac{\mu_{nu}}{L}\frac{kT}{n_q}\int_{n_{u,s}}^{n_{u,d}}\left(\frac{e^{n_u/n_q}}{e^{n_u/n_q}-1}\right)n_u dn_u}_{J_{IV}} - \underbrace{\frac{\mu_{nl}}{L}\frac{kT}{n_q}\int_{n_{u,s}}^{n_{u,d}}\left(\frac{e^{n_l/n_q}}{e^{n_l/n_q}-1}\right)n_l dn_l}_{J_V}$$
$$- \underbrace{\frac{\mu_{nl}}{L}\frac{q^2}{C_{ox}}\int_{n_{u,s}}^{n_{u,d}} n_l dn_u}_{J_{VI}} - \underbrace{\frac{\mu_{nu}}{L}\frac{q^2}{C_{ox}}\int_{n_{l,s}}^{n_{l,d}} n_u dn_l}_{J_{VII}} - \underbrace{\frac{2\mu_{nu}q\alpha}{3\epsilon_{GaN}L}\int_{n_{l,s}}^{n_{l,d}}\left(\frac{qn_l+qn_{buf}}{\epsilon_{GaN}}\right)^{-\frac{1}{3}} n_u dn_l}_{J_{VIII}} \quad (25)$$

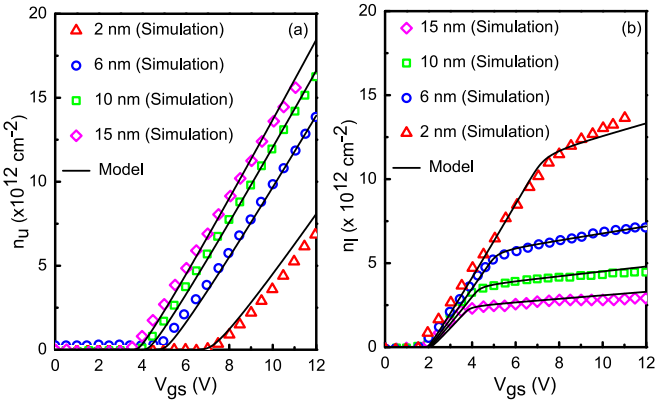

FIGURE 3. Comparison of modeled 2DEG density profiles of (a) the upper channel and (b) the lower channel with respect to TCAD characteristics [21], as a function of the gate-source voltage for different values of t_{GaN}. Charge screening of the lower channel at the onset of the upper channel, as predicted by TCAD results, is reproduced qualitatively as well as quantitatively by the model.

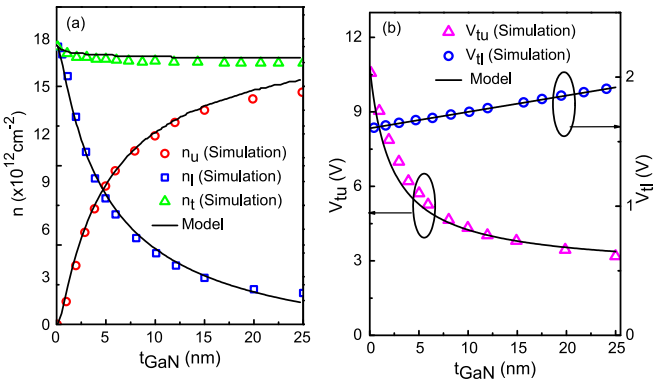

FIGURE 4. (a) Comparison of modeled 2DEG density profiles of the upper channel, the lower channel and the total ($n_t = n_l + n_u$) versus TCAD characteristics [21], as a function of t_{GaN} for a fixed gate-source voltage of 10 V. On reducing t_{GaN}, proximity of the negative polarization charge at the upper AlN surface to the upper channel increases the barrier height at upper channel and therefore decreases n_u, which in turn leads to a poor screening of the lower channel, as indicated by an increased n_l.
(b) Threshold voltage of the upper channel (V_{tu}) and the lower channel (V_{tl}) as a function of t_{GaN}, compared with TCAD data [21].

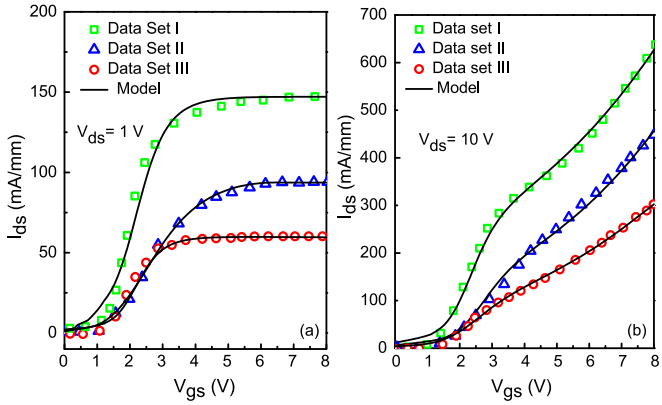

FIGURE 5. Comparison of transfer characteristics from the proposed model and experimental results from data set I, II and III at fixed drain voltage: (a) V_{ds} = 1V (b) V_{ds} = 10V.

any further gate electrostatic influence. As such, marginal increase in n_l is observed for V_{gs} values beyond V_{T}^{u}.

Fig. 3 also shows the variation in n_u and n_l for different t_{GaN} values. For the upper channel, progressively decreasing t_{GaN} has an increasing effect on V_{T}^{u}, in accordance with (18) whereas the impact of reducing the upper GaN layer thickness is two-fold in case of n_l. Small t_{GaN} strengthens the gate electrostatic control on the lower channel due to capacitive action, therefore necessitating higher screening voltages before hitting the plateau. Additionally, the increased gate control in smaller t_{GaN} leads to an increased value of saturation n_l values [23], as indicated in Fig. 3b.

The opposite variations in n_u and n_l to changes in t_{GaN} are also presented in Fig. 4a through overlays of TCAD and proposed model simulations. The total carrier density (n_t) remains almost constant, showing an agreement with results found in the literature [21]. Fig. 4b demonstrates the normally-off nature of the DC-GaN-HEMT for variable t_{GaN}, as validated by overlays of modeled V_{T}^{u} and V_{T}^{l} with TCAD characteristics. V_{T}^{u} is seen to increase with decreasing t_{GaN}, which is primarily due to an increased proximity of the net negative polarization charge at the upper GaN/AlN interface and the subsequent increase in the barrier height at upper channel. V_T^l, on the other hand, increases with increasing t_{GaN} due to decrease in capacitive coupling between the gate and the lower channel. However, the rate of change of V_T^l with t_{GaN} is fairly low, as it is dominated by the polarization dynamics of the lower channel, which remains unaltered. The different behavior of V_T^u and V_T^l as a function of t_{GaN} is also observed in Fig. 3.

B. CURRENT AND CAPACITANCES

Finally, the model validation against reported experimental data, which is divided into data sets - I [10], II [26] and III [26], is carried out in this section. The physical dimension parameters of the DC-GaN-HEMTs corresponding to these experimental data sets as well as their extracted model parameters are tabulated in Table 3. Data sets I and II differ by gate to source length, while II and III differ by upper GaN layer thickness. Fig. 5a and Fig. 5b shows overlays of modeled and experimental transfer characteristics at two different values of drain voltage, $V_{\mathrm{ds}} = 1$ V and 10 V respectively. Fig. 6 illustrates a good agreement between the model and experimental data set I transconductance characteristics, accurately predicting the V_{ds}-dependent double-peaked or single-peaked transconductance behavior, typical of DC-GaN-HEMTs.

The output characteristics of experimental data sets are validated against the model simulations in Fig. 7(a–c), for an array of V_{gs} values. Fig. 7d illustrates an accurate match of the R_{ON} between the model and the data sets for a fixed gate voltage $V_{\mathrm{gs}} = 8$ V.

The model presented above, being a charge-based model, can also be used to plot the capacitance-voltage (C–V)

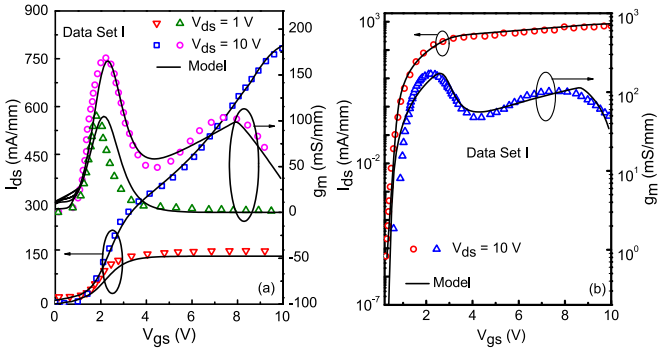

FIGURE 6. Transfer characteristics at fixed values of drain voltage, V_{ds} = 10V and 1V, obtained from analytical model and compared with experimental data set I shown in (a) Linear scale (b) Logarithmic scale. Twin peaks as observed from transconductance (g_m) versus V_{gs} plot, highlight the double channel characteristics.

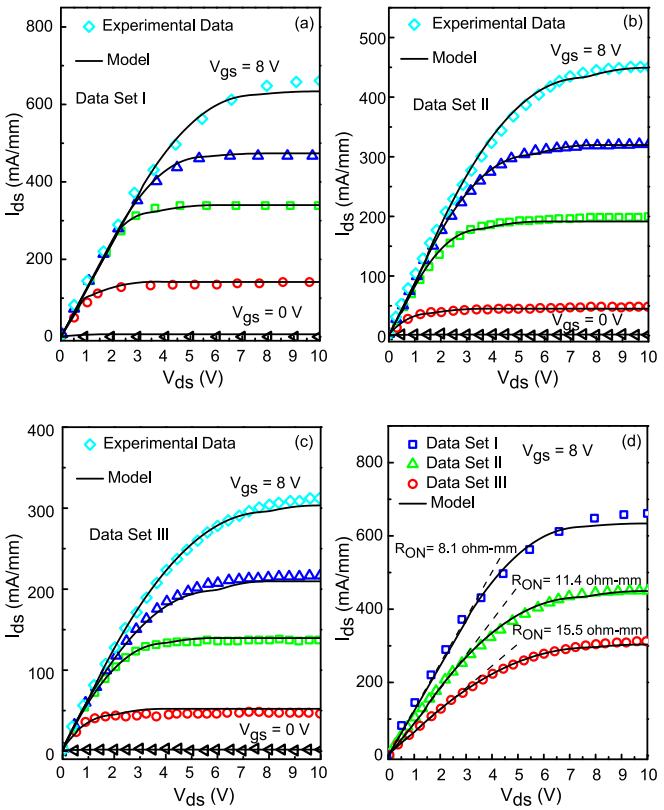

FIGURE 7. Output characteristics obtained from analytical model and compared with the experimental results of (a) data set I, (b) data set II (a) data set III. (d) Compares output characteristic at V_{gs} = 8V from the proposed model with the experimental data set I, II and III. Extracted values of R_{ON} from the model are 8.1 Ω−mm, 11.4 Ω−mm and 15.5 Ω−mm corresponding to data sets I, II and III, respectively.

TABLE 3. Experimental data sets used in Fig. 5, Fig. 6, and Fig. 7.

Parameter (symbol) (unit)	Data set I [10]	Data set II [26]	Data set III [26]
Thickness of upper GaN layer (t_{GaN}) (nm)	6	6	10
Thickness of Al_2O_3 gate dielectric (t_{ox}) (nm)	18	18	18
Intrinsic gate length (L) (μm)	1.5	1.5	1.5
Source to gate length (L_S) (μm)	2	3	3
Gate to drain length (L_D) (μm)	15	15	15
Thickness of AlN layer (t_{AlN}) (nm)	1.5	1.5	1.5
Lower Channel electron mobility (μ_{nl}) (cm^2/V.s)	2080	2080	1811
Upper Channel electron mobility (μ_{nu}) (cm^2/V.s)*	1000	1000	800

*Model Extracted Value

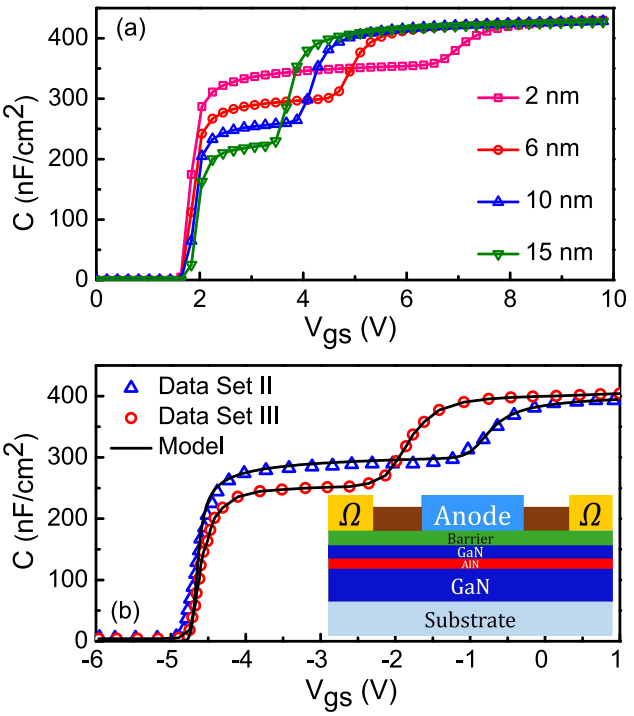

FIGURE 8. (a) *C-V* characteristic obtained from the model for different values of t_{GaN}. (b) Comparison of modeled *C-V* characteristics and the experimental data corresponding to data sets II and III of the DC-GaN Schottky-barrier diode.

behavior of DC-GaN-HEMTs. The charge densities obtained in (15) and (16) can be integrated along the channel from source to drain to yield the total channel charges, which can be subsequently used to calculate the capacitance. *C–V* characteristics, predicted by the model, for different values of t_{GaN} are shown in Fig. 8. The plots clearly exhibit double-hump features each corresponding to a channel, as would be expected of DC-GaN-HEMTs, arising at V_T^l and V_T^u values. The decreased lower-humps on increasing t_{GaN}, seen in Fig. 8a, are due to decreased capacitive coupling between the gate and the lower channel, which also result in a slight increase in V_T^l as advocated in Fig. 4b earlier. As the upper channel turns on, the capacitance reaches the maximum value of C_{ox} regardless of the t_{GaN} value, while the lower channel remains screened.

Fig. 8b shows the correlation between modeled and experimental *C–V* characteristics of DC-GaN Schottky-barrier

diodes [26] with different values of t_{GaN}, where the inset indicates the arrangement of the various layers in the DC-GaN Schottky-barrier structure used here for validation.

V. CONCLUSION

A charge-based model was presented and validated for DC-GaN-HEMTs. The model relies on the calculation of charge densities for both the channels obtained by solving the Schrödinger and Poisson equations. Fermi-Dirac statistics is taken into consideration for carrier distribution while drift-diffusion formalism is invoked for transport. Strong agreement is observed between the model and the experimental characteristics through which the model validates the features that are typical of DC-GaN-HEMTs such as normally off behavior, twin-peaked transconductance and double-humped capacitances. More importantly, the model's geometrical scalability is also demonstrated against TCAD wherein accurate reproduction of threshold voltages, sheet charge densities and capacitances are observed for an array of GaN and AlN thicknesses, making the model an important step towards realizing an optimized DC-GaN-HEMT structure.

APPENDIX
EXPRESSION OF n_u IN TERMS OF n_l

Differentiating (15) with respect to n_l, we obtain

$$\frac{dE_f}{dn_l} = \frac{q^2}{C_{ox}}\left(1+\frac{dn_u}{dn_l}\right) + \frac{kT}{n_q}\frac{e^{n_u/n_q}}{e^{n_u/n_q}-1}\frac{dn_u}{dn_l} + \frac{2}{3}\alpha\frac{q}{\epsilon_{GaN}}\left(\frac{qn_l+qn_{buf}}{\epsilon_{GaN}}\right)^{-\frac{1}{3}} \quad (32)$$

From (24) and (32), eliminating dE_f/dn_l and separating the variables yields

$$\frac{kT}{n_q}\frac{e^{n_u/n_q}}{e^{n_u/n_q}-1}dn_u = \frac{kT}{n_q}\frac{e^{n_l/n_q}}{e^{n_l/n_q}-1}dn_l + q^2\left(\frac{1}{C_{GaN}}+\frac{1}{C_{AlN}}\right)dn_l \quad (33)$$

Considering $n_u(x) = n_u$ and $n_l(x) = n_l$ be the channel charge densities at any arbitrary point x along the channel, integration of (33) from source end ($n_u(0) = n_{u,s}$, $n_l(0) = n_{l,s}$) to point x as

$$\frac{kT}{n_q}\int_{n_{u,s}}^{n_u}\frac{e^{n_u/n_q}}{e^{n_u/n_q}-1}dn_u = \frac{kT}{n_q}\int_{n_{l,s}}^{n_l}\frac{e^{n_l/n_q}}{e^{n_l/n_q}-1}dn_l + q^2\left(\frac{1}{C_{GaN}}+\frac{1}{C_{AlN}}\right)\int_{n_{l,s}}^{n_l}dn_l \quad (34)$$

gives (30).

REFERENCES

[1] Y. Okamoto, A. Wakejima, Y. Ando, T. Nakayama, K. Matsunaga, and H. Miyamoto, "100 W C-band single-chip GaN FET power amplifier," *Electron. Lett.*, vol. 42, no. 5, pp. 283–285, Mar. 2006, doi: 10.1049/el:20064067.

[2] V. Kumar, A. Kuliev, T. Tanaka, Y. Otoki, and I. Adesida, "High transconductance enhancement-mode AlGaN/GaN HEMTs on SiC substrate," *Electron. Lett.*, vol. 39, no. 24, pp. 1758–1760, Nov. 2003, doi: 10.1049/el:20031124.

[3] Y. Uemoto *et al.*, "A normally-off AlGaN/GaN transistor with $R_{on}A$=2.6mΩcm^2 and BV_{ds} = 640V using conductivity modulation," in *Proc. IEEE IEDM*, San Francisco, CA, USA, Dec. 2006, pp. 1–4, doi: 10.1109/IEDM.2006.346930.

[4] S. D. Gupta *et al.*, "Positive threshold voltage shift in AlGaN/GaN HEMTs and e-mode operation by Al_xTi_{1-x} O based gate stack engineering," *IEEE Trans. Electron Devices*, vol. 66, no. 6, pp. 2544–2550, Jun. 2019, doi: 10.1109/TED.2019.2908960.

[5] R. Wang, Y. Cai, C.-W. Tang, K. M. Lau, and K. J. Chen, "Enhancement-mode Si_3N_4/AlGaN/GaN MISHFETs," *IEEE Electron Device Lett.*, vol. 27, no. 10, pp. 793–795, Oct. 2006, doi: 10.1109/LED.2006.882522.

[6] W. Huang, Z. Li, T. P. Chow, Y. Niiyama, T. Nomura, and S. Yoshida, "Enhancement-mode GaN hybrid MOS-HEMTS with r_{on},sp of 20 mω-cm^2," in *Proc. ISPSD*, Orlando, FL, USA, May 2008, pp. 295–298, doi: 10.1109/ISPSD.2008.4538957.

[7] J. J. Freedsman *et al.*, "Normally-OFF Al_2O_3/AlGaN/GaN MOS-HEMT on 8 in. Si with low leakage current and high breakdown voltage (825 V)," *Appl. Phys. Exp.*, vol. 7, no. 4, Apr. 2014, Art. no. 041003, doi: 10.7567/APEX.7.041003.

[8] B. Lu, O. I. Saadat, and T. Palacios, "High-performance integrated dual-gate AlGaN/GaN enhancement-mode transistor," *IEEE Electron Device Lett.*, vol. 31, no. 9, pp. 990–992, Sep. 2010, doi: 10.1109/LED.2010.2055825.

[9] L. Wang *et al.*, "The plasmonic resonant absorption in GaN double-channel high electron mobility transistors," *Appl. Phys. Lett.*, vol. 99, no. 6, pp. 1–3, Aug. 2011, doi: 10.1063/1.3619842

[10] J. Wei *et al.*, "Low on-resistance normally-off GaN double-channel metal–oxide–semiconductor high-electron-mobility transistor," *IEEE Electron Device Lett.*, vol. 36, no. 12, pp. 1287–1290, Dec. 2015, doi: 10.1109/LED.2015.2489228.

[11] J. Wei *et al.*, "Enhancement-mode GaN double-channel MOS-HEMT with low on-resistance and robust gate recess," in *IEDM Tech. Dig.*, Washington, DC, USA, Dec. 2015, pp. 225–228, doi: 10.1109/IEDM.2015.7409662.

[12] S. A. Ahsan, S. Ghosh, K. Sharma, A. Dasgupta, S. Khandelwal, and Y. S. Chauhan, "Capacitance modeling in dual field-plate power GaN HEMT for accurate switching behavior," *IEEE Trans. Electron Devices*, vol. 63, no. 2, pp. 565–572, Feb. 2016, doi: 10.1109/TED.2015.2504726.

[13] S. A. Ahsan, S. Ghosh, S. Khandelwal, and Y. S. Chauhan, "Analysis and modeling of cross-coupling and substrate capacitances in GaN HEMTs for power-electronic applications," *IEEE Trans. Electron Devices*, vol. 64, no. 3, pp. 816–823, Mar. 2017, doi: 10.1109/TED.2017.2654264.

[14] S. A. Ahsan, S. Ghosh, S. Khandelwal, and Y. S. Chauhan, "Pole-zero approach to analyze and model the kink in gain-frequency plot of GaN HEMTs," *IEEE Microw. Wireless Compon. Lett.*, vol. 27, no. 3, pp. 266–268, Mar. 2017, doi: 10.1109/LMWC.2017.2661710.

[15] S. A. Ahsan, A-U.-H. Pampori, S. Ghosh, S. Khandelwal, and Y. S. Chauhan, "A new small-signal parameter extraction technique for large gate-periphery GaN HEMTs," *IEEE Microw. Wireless Compon. Lett.*, vol. 27, no. 10, pp. 918–920, Oct. 2017, doi: 10.1109/LMWC.2017.2746661.

[16] S. A. Ahsan, S. Ghosh, S. Khandelwal, and Y. S. Chauhan, "Physics-based multi-bias RF large-signal GaN HEMT modeling and parameter extraction flow," *IEEE J. Electron Devices Soc.*, vol. 5, no. 5, pp. 310–319, Sep. 2017, doi: 10.1109/JEDS.2017.2724839.

[17] S. Khandelwal *et al.*, "ASM GaN: Industry standard model for GaN RF and power devices—Part 1: DC, CV, and RF model," *IEEE Trans. Electron Devices*, vol. 66, no. 1, pp. 80–86, Jan. 2019.

[18] U. Radhakrishna, P. Choi, and D. A. Antoniadis, "Facilitation of GaN-Based RF- and HV-Circuit Designs Using MVS-GaN HEMT compact model," *IEEE Trans. Electron Devices*, vol. 66, no. 1, pp. 95–105, Jan. 2019, doi: 10.1109/TED.2018.2848721.

[19] U. Radhakrishna, S. Lim, P. Choi, T. Palacios, and D. Antoniadis, "GaNFET compact model for linking device physics, high voltage circuit design and technology optimization," in *IEDM Tech. Dig.*, Washington, DC, USA, Dec. 2015, pp. 1–4, doi: 10.1109/IEDM.2015.7409664.

[20] U. Radhakrishna, P. Choi, S. Goswami, L.-S. Peh, T. Palacios, and D. A. Antoniadis, "MIT virtual source GaNFET-RF compact model for GaN HEMTs: From device physics to RF frontend circuit design and validation," in *IEDM Tech. Dig.*, San Francisco, CA, USA, Dec. 2014, pp. 1–4, doi: 10.1109/IEDM.2014.7047034.

[21] J. Wei, M. Zhang, B. Li, X. Tang, and K. J. Chen, "An analytical investigation on the charge distribution and gate control in the normally-off GaN double-channel MOS-HEMT," *IEEE Trans. Electron Devices*, vol. 65, no. 7, pp. 2757–2764, Jul. 2018, doi: 10.1109/TED.2018.2831246.

[22] I. K. M. R. Rahman, M. I. Khan, M. Mahdia, and Q. D. M. Khosru, "Analytical modeling of electrostatic characteristics of enhancement mode GaN double channel HEMT," in *Proc. 13th IEEE Nanotechnol. Mater. Devices Conf.*, Portland, OR, USA, Oct. 2018, pp. 1–4, doi: 10.1109/NMDC.2018.8605851.

[23] I. K. M. R. Rahman, M. I. Khan, and Q. D. M. Khosru, "A rigorous investigation of electrostatic and transport phenomena of GaN double-channel HEMT," *IEEE Trans. Electron Devices*, vol. 66, no. 7, pp. 2923–2931, Jul. 2019, doi: 10.1109/TED.2019.2915837.

[24] O. Ambacher *et al.*, "Two-dimensional electron gases induced by spontaneous and piezoelectric polarization charges in N- and Ga-face AlGaN/GaN heterostructures," *J. Appl. Phys.*, vol. 85, no. 6, pp. 3222–3233, 1999, doi: 10.1063/1.369664.

[25] T.-H. Hung, P. S. Park, S. Krishnamoorthy, D. N. Nath, and S. Rajan, "Interface charge engineering for enhancement-mode GaN MISHEMTs," *IEEE Electron Device Lett.*, vol. 35, no. 3, pp. 312–314, Mar. 2014, doi: 10.1109/LED.2013.2296659.

[26] J. Wei, J. Lei, X. Tang, B. Li, S. Liu, and K. J. Chen, "Channel-to-channel coupling in normally-off GaN double-channel MOS-HEMT," *IEEE Electron Devices Lett.*, vol. 39, no. 1, pp. 59–62, Jan. 2018, doi: 10.1109/LED.2017.2771354.

[27] M. Delagebeaudeuf and N. T. Linh, "Metal-(n) AlGaAs-GaAs two-dimensional electron gas FET," *IEEE Trans. Electron Devices*, vol. 29, no. 6, pp. 955–960, Jun. 1982, doi: 10.1109/T-ED.1982.20813.

[28] H. K. Kwon *et al.*, "Radiative recombination of two dimensional electrons in a modulation doped $Al_{0.37}Ga_{0.63}N$/GaN single heterostructure," *Appl. Phys. Lett.*, vol. 75, no. 18, pp. 2788–2790, Nov. 1999, doi: 10.1063/1.125150.

[29] S. M. Sze and K. K. Ng, *Physics of Semiconductor Devices*. Hoboken, NJ, USA: Wiley, 2006.

[30] E. G. Marin, S. J. Bader, and D. Jena, "A new holistic model of 2-D semiconductor FETs," *IEEE Trans. Electron Devices*, vol. 65, no. 3, pp. 1239–1245, Mar. 2018, doi: 10.1109/TED.2018.2797172.